

Structure and energetics of grain boundaries in self-assembled double-gyroid block copolymer networks

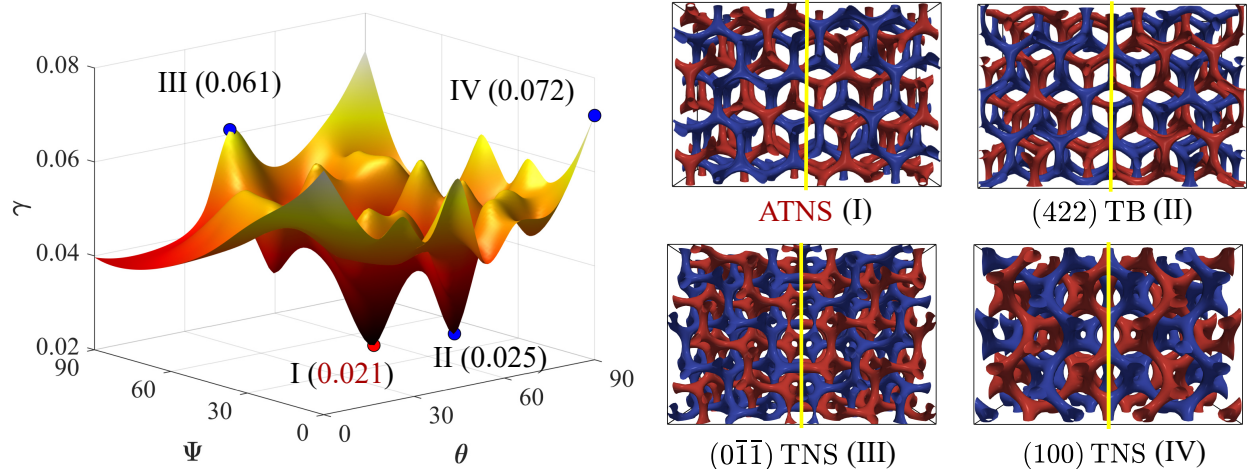
Jing Chen,^{†,‡} Aiping Zhu,^{†,‡} Dan Wei,^{*,†} An-Chang Shi,^{*,¶} and Kai Jiang^{*,†}

[†]*Hunan Key Laboratory for Computation and Simulation in Science and Engineering, Key Laboratory of Intelligent Computing and Information Processing of Ministry of Education, School of Mathematics and Computational Science, Xiangtan University, Xiangtan, Hunan, China, 411105*

[‡]*These authors contributed equally to this work.*

[¶]*Department of Physics and Astronomy, McMaster University, Hamilton, Ontario, L8S4M1, Canada*

E-mail: danwei@xtu.edu.cn; shi@mcmaster.ca; kaijiang@xtu.edu.cn



Graphic Table of Contents.

Abstract

Grain boundaries (GBs) are ubiquitous defects in crystalline materials. However, they remain less explored in block copolymer ordered phases. Here, we develop a self-consistent field theory framework to investigate GB structure and energetics in double-gyroid (DG) diblock copolymer networks. The GB energy landscape is obtained as a function of GB orientation, which reveals multiple local minima representing distinct network-switching GBs. Remarkably, the global minimum is a previously unidentified asymmetric-tilt network-switching GB (ATNS), exhibiting a lower energy than the experimentally observed (422) twin boundary (TB). Comparative analyses of representative low- (ATNS, (422) TB) and high-energy twist ((01̄1̄), (100) TNSs) GBs reveal that, unlike enthalpy-dominated hard matter, GB stability in DG networks is predominantly entropy-driven. Twist-type GBs generate new nodes and disrupt nodal coplanarity, causing chain packing frustration and large entropy penalties. Conversely, the ATNS preserves favorable network connectivity and minimizes conformational constraints on polymer chains, making it the energetically preferred GB.

Introduction

Block copolymers (BCPs) can self-assemble into various ordered structures via microphase separation of chemically immiscible blocks.¹ Beyond the classical lamellar, cylindrical, and spherical phases,¹ BCPs are also known to form complex three-dimensional network structures, including the double gyroid (DG),^{2,3} double diamond (DD),^{4,5} and Fddd phases.^{6,7} These network phases have attracted sustained interest due to their potential applications in photonic crystals,⁸⁻¹⁰ ion transport media^{11,12} and plasmonic metamaterials.¹³⁻¹⁵ However, in practical applications, BCPs rarely form ideal single-crystalline structures. Inevitable impurities during synthesis, together with kinetic limitations during microphase separation and grain growth, lead to the formation of various defects.¹⁶⁻²¹ Among these, grain boundaries (GBs) are the ubiquitous two-dimensional defects, which are interfaces separating grains of the same phase with different orientations. Their presence disrupts the structural symmetry, and can strongly influence the macroscopic properties of materials.

In hard matter such as metals and alloys, the energetics of GBs is primarily governed by inter-atomic interactions.²²⁻²⁴ Strong interatomic bonding and large elastic moduli impose stringent lattice constraints, so that even angstrom-scale atomic displacements from ideal lattice sites incur substantial energetic penalties.²⁵ As a consequence, GB energies are primarily determined by geometric lattice mismatch and elastic distortion.²² High-symmetry twin boundaries (TBs), which minimize atomic misfit and strain, emerge as the representative low-energy configurations in hard matter.²⁶⁻²⁹ In contrast, the networked phases of BCPs form on nanometer-to-micrometer length scales. Their stability originates not from strong chemical bonding, but rather from a subtle competition between weak non-covalent interactions (e.g., van der Waals forces) and the conformational entropy of the polymer chains. The intrinsic plasticity of “soft” lattices affords BCP networks high geometric deformability, continuous skeletal connectivity, and significant topological freedom. During GB formation, geometric incompatibility and elastic penalties are mitigated by long relaxation times, chain conformational adjustments, and network reconfigurations, rather than being constrained

by strict lattice matching. Consequently, the energy landscape of GBs in BCP networked phases is fundamentally reshaped. Symmetry-based selection rules, traditionally applied to hard matter, may no longer suffice as a standalone metric for identifying low-energy GB configurations. The flexibility of GBs in soft matter raises a fundamental question: beyond the experimentally observed TBs, do other configurations with even lower GB energies exist, and what physical mechanisms govern their stability in BCP network phases? To date, these issues remain largely unexplored.

Experimentally, early studies of GBs in BCPs primarily focused on lamellar phases, where twist and tilt GBs were characterized via transmission electron microscopy.^{30–34} In contrast, studies of GBs in complex networked phases remain limited, largely centered on the structural characterization and geometric analysis of TBs in DG and DD phases.^{35–40} Non-twin GBs in these networked structures have received far less attention and remain largely unexplored. Theoretically, previous studies of network-phase GBs have primarily relied on minimal surface models^{36,41} or Landau-type theories.^{42,43} While these approaches effectively capture geometric features, their application to BCP systems is not straightforward.

For inhomogeneous polymeric systems, the self-consistent field theory (SCFT) provides a powerful framework and offers the distinct advantage of simultaneously capturing polymer chain conformations, entropy and interaction energies with well-defined physical parameters.⁴⁴ Although SCFT has been extensively applied to periodic structures^{1,45,46} and even quasicrystals,^{47,48} its application to the study of GBs remains notably rare. To date, SCFT-based GB research is restricted to simple lamellar phases,^{31,49–53} whereas the GBs in complex networked phases have yet to be explored.

In this study, we perform a systematic theoretical investigation of GBs in BCP networked phases, aiming to gain an understanding of their structures and stability mechanisms. By developing a SCFT framework tailored for GB computations, we construct a comprehensive GB energy landscape in the orientation space (θ, Ψ) , where each point represents a distinct orientation of the GB. This landscape captures rich GB structures spanning both tilt and

twist configurations and enables the identification of novel low-energy GBs. Interestingly, our results reveal that the experimentally observed (422) TB is not the global minimum. Instead, a previously unidentified asymmetric-tilt network-switching GB (ATNS) emerges as a global energy minimizer. To elucidate the underlying mechanism, we investigate a representative set of GBs, including the low-energy ATNS and (422) TB, together with two higher-energy twist GBs ($(0\bar{1}\bar{1})$) and (100) TNSs) for comparison. Analyses of entropy and interaction energies, chain conformations, network topologies, and geometric deformations demonstrate that, GB stability in BCP network phases is primarily governed by entropy penalties associated with node formation and coplanarity, in stark contrast to the enthalpy-dominated behavior typically found in hard materials.

Theoretical Framework

This work focuses on the spontaneous formation of a GB when two grains of the same phase with different orientations come into contact. Our computational framework is illustrated schematically in Fig. 1. The two grains, each with a predefined orientation, are positioned in the two opposing half-spaces, grain 1 at $x \leq -L_x/2$ and grain 2 at $x \geq L_x/2$. The intermediate region $-L_x/2 < x < L_x/2$ is made sufficiently large to allow for the full relaxation of the GB. SCFT calculations are performed in the rectangular box of volume $V = L_x \times L_y \times L_z$. To fix the terminal structures to their corresponding grains, anchoring boundary conditions are imposed at $x = \pm L_x/2$, while periodic boundary conditions are applied in the y - and z -directions. Under this setup, the grains on both sides evolve toward each other along the x -direction. Due to the difference of crystallographic orientations, they cannot achieve a defect-free connection upon meeting, resulting in the formation of a GB within a transition zone indicated by the gray region in Fig. 1, where the network topology, chain conformation, and local geometric structure undergo a synergistic rearrangement to accommodate the orientation mismatch.

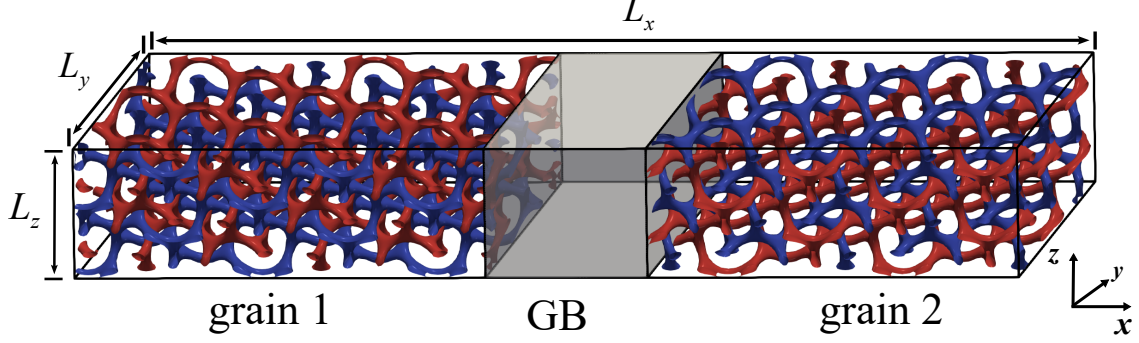


Figure 1: Schematic of the computational setup.

SCFT model for GBs

We consider an incompressible melt of n flexible AB diblock copolymers in the rectangular box. Each polymer chain consists of two conformationally symmetric A- and B-blocks. The degree of polymerization of the A-block is denoted by $N_A = fN$, where f represents the volume fraction of the A-block, and N is the total degree of polymerization of the chain. The degree of polymerization of the B-block is given by $N_B = (1 - f)N$. The flexible blocks are modeled as Gaussian chains, and their propagators obey the modified diffusion equations (MDEs),

$$\begin{aligned} \frac{\partial}{\partial s} q(\mathbf{r}, s) &= \nabla_{\mathbf{r}}^2 q(\mathbf{r}, s) - w_A(\mathbf{r}) q(\mathbf{r}, s), & 0 \leq s \leq f, \\ \frac{\partial}{\partial s} q(\mathbf{r}, s) &= \nabla_{\mathbf{r}}^2 q(\mathbf{r}, s) - w_B(\mathbf{r}) q(\mathbf{r}, s), & f \leq s \leq 1, \end{aligned} \quad (1)$$

where $q(\mathbf{r}, s)$ represents the probability of the s -th chain segment at spatial position \mathbf{r} in mean fields $w_\alpha(\mathbf{r})$, $\alpha \in \{A, B\}$. The backward propagator $q^\dagger(\mathbf{r}, s)$ is defined analogously, satisfying similar MDEs,

$$\begin{aligned} \frac{\partial}{\partial s} q^\dagger(\mathbf{r}, s) &= \nabla_{\mathbf{r}}^2 q^\dagger(\mathbf{r}, s) - w_B(\mathbf{r}) q^\dagger(\mathbf{r}, s), & 0 \leq s \leq 1 - f, \\ \frac{\partial}{\partial s} q^\dagger(\mathbf{r}, s) &= \nabla_{\mathbf{r}}^2 q^\dagger(\mathbf{r}, s) - w_A(\mathbf{r}) q^\dagger(\mathbf{r}, s), & 1 - f \leq s \leq 1. \end{aligned} \quad (2)$$

To fix the crystallographic orientations of the two grains, inhomogeneous Dirichlet boundary conditions are imposed on the propagators along the x -direction. Meanwhile, periodic boundary conditions are applied in the y - and z -directions. Therefore, the boundary and

initial conditions are given by,

$$\begin{aligned}
q(-L_x/2, y, z, s) &= q_{\text{grain1}}(-L_x/2, y, z, s), \\
q(L_x/2, y, z, s) &= q_{\text{grain2}}(L_x/2, y, z, s), \\
q(\mathbf{r}, 0) &= 1, \\
q^\dagger(-L_x/2, y, z, s) &= q_{\text{grain1}}^\dagger(-L_x/2, y, z, s), \\
q^\dagger(L_x/2, y, z, s) &= q_{\text{grain2}}^\dagger(L_x/2, y, z, s), \\
q^\dagger(\mathbf{r}, 0) &= 1.
\end{aligned} \tag{3}$$

Using these propagators, the single-chain partition function Q and segment densities $\phi_{\alpha, \text{GB}}(\mathbf{r})$ ($\alpha \in \{\text{A}, \text{B}\}$) of GB structures can be calculated as,

$$\begin{aligned}
Q &= \frac{1}{V} \int_V q(\mathbf{r}, s) q^\dagger(\mathbf{r}, 1-s) d\mathbf{r}, \quad \forall s \in [0, 1], \\
\phi_{\text{A}, \text{GB}}(\mathbf{r}) &= \frac{1}{Q} \int_0^f q(\mathbf{r}, s) q^\dagger(\mathbf{r}, 1-s) ds, \\
\phi_{\text{B}, \text{GB}}(\mathbf{r}) &= \frac{1}{Q} \int_f^1 q(\mathbf{r}, s) q^\dagger(\mathbf{r}, 1-s) ds.
\end{aligned} \tag{4}$$

The free energy per chain in unity of $k_B T$ is obtained by ^{44,54}

$$\begin{aligned}
\frac{F_{\text{GB}}}{nk_B T} &= \frac{1}{V} \int_V \left\{ \chi N \phi_{\text{A}, \text{GB}}(\mathbf{r}) \phi_{\text{B}, \text{GB}}(\mathbf{r}) - \sum_{\alpha \in \{\text{A}, \text{B}\}} w_\alpha(\mathbf{r}) \phi_{\alpha, \text{GB}}(\mathbf{r}) \right. \\
&\quad \left. + \eta(\mathbf{r}) \left[1 - \sum_{\alpha \in \{\text{A}, \text{B}\}} \phi_{\alpha, \text{GB}}(\mathbf{r}) \right] \right\} d\mathbf{r} - \ln Q,
\end{aligned} \tag{5}$$

where T is the temperature, k_B is the Boltzmann constant, χ is the Flory-Huggins interaction parameter, and $\eta(\mathbf{r})$ is the ‘‘pressure’’ field that ensures the incompressibility of the system. The free energy per chain $F_{\text{GB}}/nk_B T$ can be divided into two parts, the segment-segment

interaction energy $F_{\text{GB}}^{\text{inter}}/nk_{\text{B}}T$ and the entropic contribution energy $-TS_{\text{GB}}/nk_{\text{B}}T$,

$$\begin{aligned} \frac{F_{\text{GB}}^{\text{inter}}}{nk_{\text{B}}T} &= \frac{1}{V} \int_V \left\{ \chi N \phi_{\text{A,GB}}(\mathbf{r}) \phi_{\text{B,GB}}(\mathbf{r}) - \sum_{\alpha \in \{\text{A,B}\}} w_{\alpha}(\mathbf{r}) \phi_{\alpha,\text{GB}}(\mathbf{r}) \right. \\ &\quad \left. + \eta(\mathbf{r}) \left[1 - \sum_{\alpha \in \{\text{A,B}\}} \phi_{\alpha,\text{GB}}(\mathbf{r}) \right] \right\} d\mathbf{r}, \\ -\frac{TS_{\text{GB}}}{nk_{\text{B}}T} &= -\ln Q. \end{aligned} \quad (6)$$

First-order variations of the free-energy functional with respect to $\eta(\mathbf{r})$, $\phi_{\text{A,GB}}(\mathbf{r})$ and $\phi_{\text{B,GB}}(\mathbf{r})$ lead to the SCFT equations,

$$\begin{aligned} \phi_{\text{A,GB}}(\mathbf{r}) + \phi_{\text{B,GB}}(\mathbf{r}) &= 1, \\ w_{\text{A}}(\mathbf{r}) &= \chi N \phi_{\text{B,GB}}(\mathbf{r}) + \eta(\mathbf{r}), \\ w_{\text{B}}(\mathbf{r}) &= \chi N \phi_{\text{A,GB}}(\mathbf{r}) + \eta(\mathbf{r}). \end{aligned} \quad (7)$$

Numerical Methods

Starting from an initial GB configuration, the SCFT equations are solved iteratively to obtain the equilibrium GB structures. Each iteration involves solving the MDEs (Eq. (1) and (2)) to obtain the propagators, which are then used to compute the single-chain partition function, segment densities (Eq. (4)), free energy (Eq. (5)), and update the mean fields (Eq. (7)). This process is repeated until the free energy difference between two consecutive iterations falls below a prescribed tolerance.

The initial GB configuration is constructed by joining two grains with different orientations across the $x = 0$ plane. Specifically, the segment density of the A-block in the bulk phase, $\phi_{\text{A,bulk}}(\mathbf{r})$, is first obtained through SCFT calculations within a unit cell.^{55,56} Grains with different orientations are then constructed by applying rigid-body rotations $\mathbf{R}_m \in \text{SO}(3)$ ($m = 1, 2$) to the $\phi_{\text{A,bulk}}(\mathbf{r})$. The segment density of the rotated grain m ,

$\phi_{\text{A, grain}}^{\mathbf{R}_m}(\mathbf{r})$, is expressed as,

$$\phi_{\text{A, grain}}^{\mathbf{R}_m}(\mathbf{r}) = \phi_{\text{A, bulk}}(\mathbf{R}_m^T \mathbf{r}) = \sum_{\mathbf{h} \in \mathbb{Z}^3} \hat{\phi}_{\text{A, bulk}}(\mathbf{h}) e^{i(\mathbf{R}_m \mathcal{B} \mathbf{h})^T \mathbf{r}}, \quad (8)$$

where \mathcal{B} denotes the primitive reciprocal lattice.

In the current study, we focus on the case where the two grains share a common period in the y - z plane. This case holds if the columns of the matrix $(\tilde{\mathbf{R}}_1^T \mathcal{B}, \tilde{\mathbf{R}}_2^T \mathcal{B})$ are linearly independent over the rational number field. Here, $\tilde{\mathbf{R}}_m$ ($m = 1, 2$) denotes the matrix formed by selecting the last two columns of the rotated matrix \mathbf{R}_m , and $\tilde{\mathbf{R}}_m^T \mathcal{B}$ represents the reciprocal lattice vectors of grain m projected onto the y - z plane.

The initial segment density of the A-block in GB structure, $\phi_{\text{A, GB}}(\mathbf{r})$, is generated by a weighted combination of the two rotated grains,

$$\phi_{\text{A, GB}}(\mathbf{r}) = (1 - c(x)) \phi_{\text{A, grain}}^{\mathbf{R}_1}(\mathbf{r}) + c(x) \phi_{\text{A, grain}}^{\mathbf{R}_2}(\mathbf{r}), \quad (9)$$

where the smooth function $c(x)$ is given by,

$$c(x) = \frac{1 + \tanh(\sigma x)}{2}, \quad (10)$$

and the parameter σ is chosen large enough such that $c(-L_x/2) = 0$ and $c(L_x/2) = 1$. The GB segment density of the B-block, $\phi_{\text{B, GB}}(\mathbf{r})$, is determined by the incompressibility condition. These segment densities provide suitable initial values for SCFT calculations of GB structures.

For solving the MDEs, we adopt periodic boundary conditions in the x -direction to approximate the inhomogeneous Dirichlet boundary condition. We will explicitly verify that this approximation does not affect the converged GB structures and the high-precision computation of GB energy. Consequently, we can treat the spatial variables using the pseudo-spectral method, while the chain contour direction is discretized by the fourth-order backward

differentiation method. Furthermore, we employ the Anderson mixing method to obtain the SCFT solutions corresponding to ordered GB structures.^{57,58} The entire algorithm is implemented in C++ language, with parallel computations performed using the FFTW-MPI package.^{59,60}

Since periodic boundary conditions are imposed along the x -direction, the equilibrium phases obtained from SCFT calculation exhibit distortions near the computational boundaries. To accurately investigate the stability of GBs, it is necessary to eliminate the deformation effects introduced by boundary conditions. To this end, we need to identify these deformation regions and exclude them from subsequent analyses. Specifically, we quantify the structural deviation along the x -direction by defining the maximum segment density difference $D(x)$ between the GB and the rotated grains, as expressed below,

$$D(x) = \begin{cases} \max_{\tilde{\mathbf{r}}} |\phi_{\text{A,GB}}(x, \tilde{\mathbf{r}}) - \phi_{\text{A}}^{R_1}(x, \tilde{\mathbf{r}})|, & -L_x/2 \leq x < 0, \\ \max_{\tilde{\mathbf{r}}} |\phi_{\text{A,GB}}(x, \tilde{\mathbf{r}}) - \phi_{\text{A}}^{R_2}(x, \tilde{\mathbf{r}})|, & 0 < x \leq L_x/2, \end{cases} \quad (11)$$

where $\tilde{\mathbf{r}} = (y, z)^T$. When the value of $D(x)$ satisfies $D(x) \leq \epsilon$ (a prescribed threshold), the local morphology is considered to be consistent with that of the corresponding bulk structure, and the region is identified as an undeformed grain region. Conversely, when $D(x)$ exceeds this threshold, the structure deviates significantly from the bulk morphology and is classified as a deformed region influenced by the GB or the imposed boundary conditions. More detailed calculations are provided in the *GB Energy* subsection.

Results and Discussion

Based on the SCFT framework described above, we systematically investigate the structure and properties of GBs in the DG phase. To search for new and more stable configurations, we construct a GB energy landscape. Geometrically, a GB structure is determined by the

relative orientation of the two grains, the normal of contact plane, and the relative interfacial translation. In this study, the contact plane normal is fixed along the x -direction. To construct coincidence site lattice GBs, we first select a set of angles $(\theta, \Psi) \in [0^\circ, 90^\circ] \times [0^\circ, 90^\circ]$ in spherical coordinates to specify a rational crystallographic direction of the unit cell, which serves as the relative rotation axis for the two grains (refer to the top-right illustration in Fig. 2 (a)). Subsequently, the spatial orientation of the unit cell is adjusted such that this rational direction is aligned either parallel (for twist-type GBs) or perpendicular (for tilt-type GBs) to the x -direction to obtain grain 1 (refer to the bottom-right illustration in Fig. 2 (a)). Grain 2 is then constructed by rotating grain 1 by an angle of π about the aligned rational axis. These two grains are joined to form an initial GB configuration, which is subsequently relaxed to reach equilibrium structure using SCFT. The GB energy γ is extracted via the linear relationship between the excess free energy and the reciprocal of the domain size along the x -direction (see *GB Energy* for further details). Through the systematic exploration of the parameter space (θ, Ψ) , we obtain the final GB energy landscape for the DG phase, which is shown in Fig. 2 (a).

The resulting energy landscape exhibits a complex and corrugated surface with multiple local minima. These minima are associated with distinct network-switching GBs, suggesting that the network switching is more favorable to the GB stability within the DG phase. Notably, the landscape reveals two pronounced minima, labeled I and II. The global minimum (I, $\gamma = 0.021$) corresponds to an asymmetric tilt network-switching GB (ATNS), which is energetically more favorable than the experimentally observed (422) TB (II, $\gamma = 0.025$), here referred to as a twist network-switching GB ((422) TNS). This finding contrasts with hard-matter systems, where symmetric TBs are typically favored, indicating a different stability mechanism for soft network GBs.

To uncover the physical origin of this stability, we select four representative network-switching GBs from the energy landscape for in-depth analysis, including the two low-energy minima (ATNS and (422) TNS) and two high-energy twist GBs ((0 $\bar{1}\bar{1}$) and (100) TNSs).

Their three-dimensional morphologies, illustrated in Fig. 2 (b), all exhibit network chirality switching across the contact plane. The geometric relations between the two grains are summarized in Tab. 1. Within the thermodynamically stable DG region ($N = 100$, $\chi = 0.14$, $0.38 \leq f \leq 0.41$), we systematically analyze these GBs from both energetic and structural perspectives, including interaction and entropy contributions, chain trajectories, network topologies, and geometric deformations.

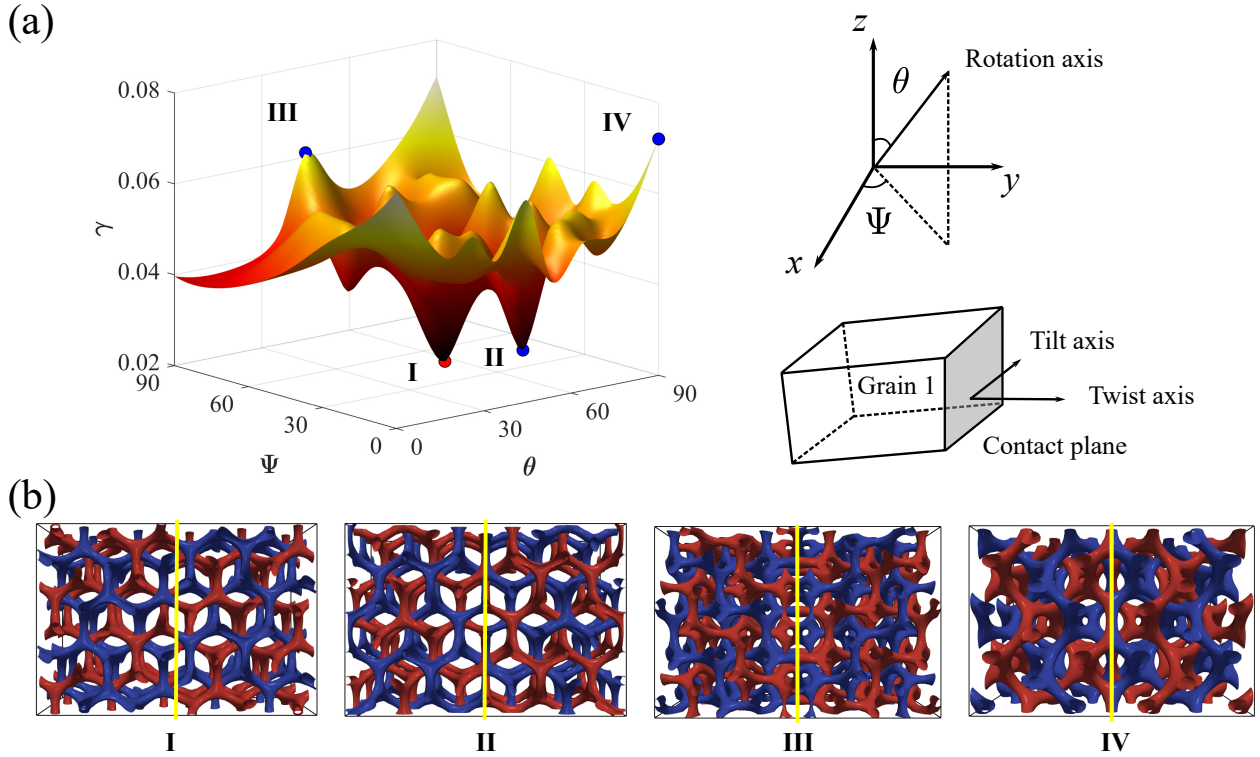


Figure 2: (a) GB energy landscape as a function of rotation-axis angles θ and Ψ at $\chi N = 14$, $f = 0.40$. The schematic diagram of the rotation axis is shown in the upper right part of the figure. Both tilt- and twist-type GBs are considered after fixing grain 1. (b) Representative GB morphologies corresponding to the labeled in (a), where ATNS (I), (422) TNS (II), (01 $\bar{1}$) TNS (III), and (100) TNS (IV), with GB energies $\gamma = 0.021$, 0.025 , 0.061 , and 0.072 , respectively. Vertical yellow lines denote the contact planes. The three-dimensional structures are visualized by isosurfaces of the A-block segment density at $\phi_{A,GB} = 0.8$, which clearly depict the network architectures. Blue and red colors are used to distinguish the left- and right-handed networks, respectively.

Table 1: Posing of two grains for the four network-switching GBs in DG phase, where a denotes the cubic unit cell size of the bulk DG.

	Two Grains	Contact Plane	Coincident Directions		Coincident Point
ATNS	grain 1	$(\bar{1}\bar{1}\bar{2})$	$[\bar{1}\bar{1}\bar{1}]$	$[\bar{1}\bar{1}0]$	$(0, 0, 0)$
	grain 2	(112)	$[\bar{1}\bar{1}\bar{1}]$	$[1\bar{1}0]$	$(0, 0, 0)$
(422) TNS	grain 1	(422)	$[1\bar{1}\bar{1}]$	$[01\bar{1}]$	$(0, 0, a/2)$
	grain 2	(422)	$[\bar{1}11]$	$[0\bar{1}1]$	$(0, 0, a/2)$
$(0\bar{1}\bar{1})$ TNS	grain 1	$(0\bar{1}\bar{1})$	$[0\bar{1}\bar{1}]$	$[\bar{1}00]$	$(0, 0, 0)$
	grain 2	$(0\bar{1}\bar{1})$	$[0\bar{1}\bar{1}]$	$[100]$	$(0, 0, 0)$
(100) TNS	grain 1	(100)	$[001]$	$[0\bar{1}0]$	$(0, 0, 0)$
	grain 2	(100)	$[00\bar{1}]$	$[010]$	$(0, 0, 0)$

GB Energy

The relative stability of the four network-switching GBs is quantified by their GB energies. The GB energy γ is defined as the excess free energy of the GB system relative to the rotated grain. For a region of length L in the x -direction, it is given by

$$\gamma = (E_{\text{GB}} - E_{\text{grain}})L, \quad (12)$$

where $E_{\text{GB}} = F_{\text{GB}}/nk_{\text{B}}T$ and $E_{\text{grain}} = F_{\text{grain}}/nk_{\text{B}}T$ are the free energies per unit volume of the GB system and the corresponding rotated grain, respectively. This relationship implies that the free energy difference scales linearly with the inverse of length,

$$E_{\text{GB}} - E_{\text{grain}} = \gamma L^{-1}, \quad (13)$$

where the slope of the linear fit yields the GB energy γ .

To ensure an accurate extraction of the GB energy, it is crucial to eliminate boundary-induced distortions arising from the imposed boundary conditions. Taking the (422) TNS at $f = 0.4$ and $\chi N = 14$ as an example, we employ Eq. (11) with a threshold of $\epsilon = 0.02$ to identify the deformed regions. As shown in Fig. 3(a), regions with $|x| > L_1$ are influenced

by boundary constraints, while the region $|x| < L_2$ corresponds to the central GB region. Therefore, only the intermediate domain $|x| \leq L_1$ is retained for the GB energy calculation. Within the window $2L_2 < L < 2L_1$, we evaluate the free energy E_{GB} for a series of lengths L by restricting the converged SCFT solutions $\phi_{\alpha, \text{GB}}(\mathbf{r}), w_{\alpha}(\mathbf{r}), Q, \alpha \in \{\text{A, B}\}$ to the interval $-L < x < L$ and substituting them into the free energy functional defined in Eq. (5). The corresponding grain free energy E_{grain} is obtained following the same procedure. The resulting free energy difference $E_{\text{GB}} - E_{\text{grain}}$ is plotted as a function of L^{-1} in Fig. 3 (b). The excellent linear scaling confirms that residual boundary effects are effectively eliminated, enabling an accurate determination of the GB energy. For the (422) TNS, the GB energy is extracted as $\gamma = 0.025$ from the slope of the linear fit (Fig. 3(b)). Under the same parameters, the ATNS, (0 $\bar{1}\bar{1}$) and (100) TNSs exhibit analogous scaling behavior, but their GB energies differ markedly. The ATNS has a lower value of $\gamma = 0.021$ (Fig. 3(c)), while the (0 $\bar{1}\bar{1}$) and (100) TNS exhibit larger GB energies of $\gamma = 0.061$ and 0.072 , respectively (Fig. 3(d)-(e)). All calculated GB energies converge within an accuracy of 10^{-4} , which is sufficient to determine the relative thermodynamic stability of these configurations.

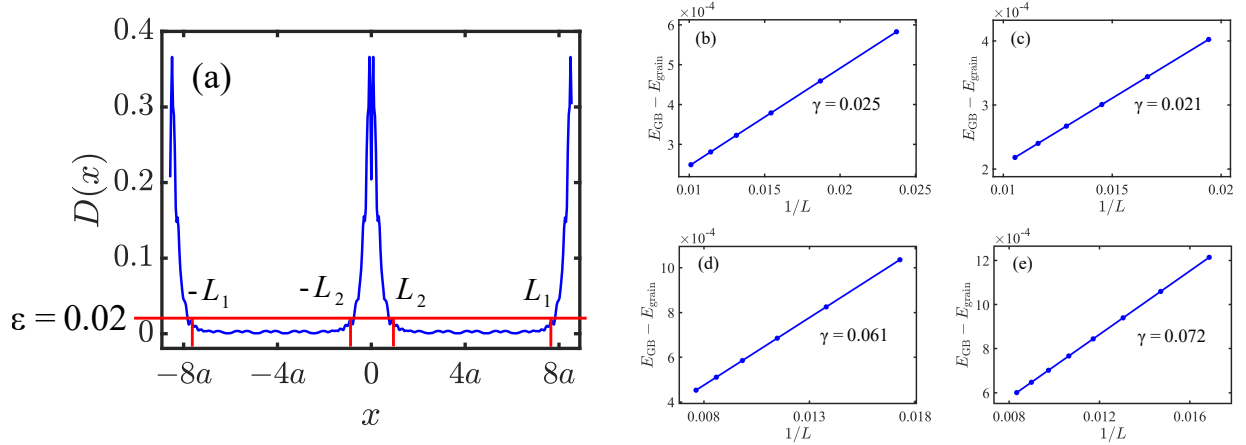


Figure 3: (a) Maximum density difference between the (422) TNS and the corresponding grains along x -direction, where $|x| < L_2$ is the the central GB region, $-L_1 \leq x \leq -L_2$ and $L_2 \leq x \leq L_1$ correspond to grain 1 and grain 2, respectively, while $|x| > L_1$ are distortion regions resulting from the boundary conditions. The optimal edge length of the bulk DG is $a = 8.5$ at $f = 0.4$.⁶¹ Free energy differences of (b) (422) TNS, (c) ATNS, (d) (0 $\bar{1}\bar{1}$) TNS and (e) (100) TNS relative to their rotated grain 1 as a function of $1/L$, where the slope of the linear fit is the GB energy γ .

Using the scaling method, the GB energies of all four structures as a function of the A-block volume fraction f are plotted in Fig. 4(a). Across the composition range $0.38 \leq f \leq 0.41$, the ATNS consistently possesses the lowest GB energy, demonstrating its superior thermodynamic stability. The (422) TNS exhibits slightly higher and comparably weak f -dependent GB energies, whereas the (100) and $(0\bar{1}\bar{1})$ TNSs are significantly less stable and exhibit greater sensitivity to composition. To elucidate the physical origin of these stability differences, we decompose the total GB energy into interaction energy (γ^{inter}) and entropy energy (γ^{entro}) contributions,

$$\begin{aligned}\gamma^{\text{inter}} &= L (F_{\text{GB}}^{\text{inter}} - F_{\text{grain}}^{\text{inter}}) / nk_{\text{B}}T, \\ \gamma^{\text{entro}} &= L [(-TS_{\text{GB}}) - (-TS_{\text{grain}})] / nk_{\text{B}}T,\end{aligned}\tag{14}$$

where $F_{\text{GB}}^{\text{inter}}/nk_{\text{B}}T$ ($F_{\text{grain}}^{\text{inter}}/nk_{\text{B}}T$) and $-TS_{\text{GB}}/nk_{\text{B}}T$ ($-TS_{\text{grain}}/nk_{\text{B}}T$) represent the interaction and entropy energies of GB structure (grain 1), respectively.

As shown in Fig. 4(b)-(c), the interaction energies of the ATNS and (422) TNS are comparable, with the ATNS even exhibiting a slightly higher interaction penalty. However, this unfavorable interaction contribution is more than offset by a substantially lower entropy penalty, which minimizes the total free energy of the ATNS. In contrast, although the (100) and $(0\bar{1}\bar{1})$ TNSs gain partial energetic advantage from reduced interaction energies, their large entropy penalties dominate, resulting in higher total GB energies. These results demonstrate that, the GB stability in BCP network phases is governed primarily by entropy rather than interaction energy, in sharp contrast to hard matter.

Chain Trajectories

The dominance of entropy in determining GB stability motivates a microscopic analysis of chain conformations and network geometry near the interface. In ideal BCP networks, polymer chains preferentially orient along the normal direction of intermaterial dividing

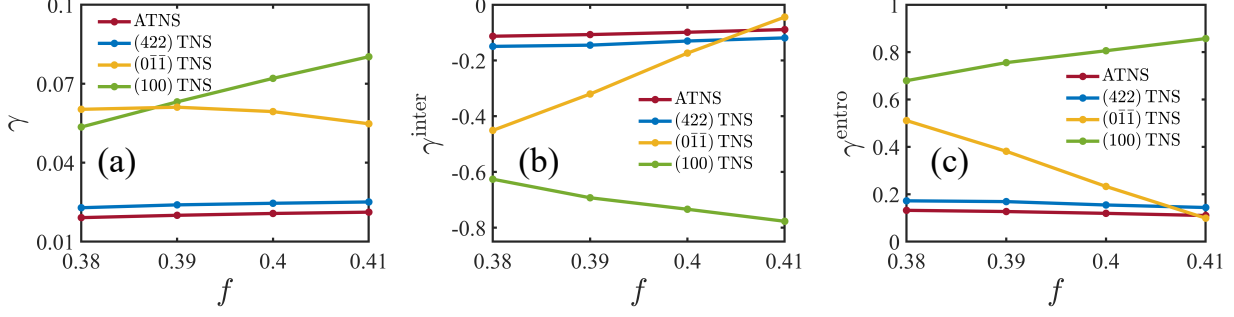


Figure 4: (a) GB energy γ , (b) interaction energy γ^{inter} , and (c) entropy energy γ^{entro} as a function of the volume fraction f .

surface (IMDS, the isosurface $\phi_A(\mathbf{r}) = 0.5$).^{62,63} This arrangement represents a relaxed conformational state with minimal packing frustration (see Fig. 5 (a1)). However, in the network-switching GBs, the geometric mismatch between the two grains is alleviated through conformational adjustment of flexible chains, leading to deviations of chain orientation from the IMDS normal direction and an associated entropy penalty (see Fig. 5 (a2)). Meanwhile, the adjustment of chain conformations is accompanied by geometric deformation of the soft network. This alters the contact patterns and distribution of A–B monomers, affecting the interaction energy of the system.

To quantify these effects, we introduce a polar order parameter to describe the average orientation of polymer chains,^{62,63} and its expression is,

$$\mathbf{P}(\mathbf{r}) = \int_0^1 \mathbf{J}(\mathbf{r}, s) ds, \quad (15)$$

where the chain flux $\mathbf{J}(\mathbf{r}, s)$ satisfies,

$$\mathbf{J}(\mathbf{r}, s) = \frac{1}{6Q} (q(\mathbf{r}, s) \nabla q^\dagger(\mathbf{r}, 1-s) - q^\dagger(\mathbf{r}, 1-s) \nabla q(\mathbf{r}, s)), \quad s \in [0, 1]. \quad (16)$$

The chain conformational frustration is characterized by the chain deviation angle θ between the normalized polar order parameter $\hat{\mathbf{P}}(\mathbf{r})$ and the unit normal vector of the IMDS $\hat{\mathbf{n}}(\mathbf{r})$ (see Fig. 5 (a2)). Meanwhile, variations in the interaction energy are quantified by the

IMDS area per unit volume A/V^L , where V^L is the volume of the measurement domain. Fig. 5 (b) visualizes the spatial distribution of these deviation angles for all four GBs. Large deviations are localized near the contact plane, where network reconnection and topological rearrangement occur.

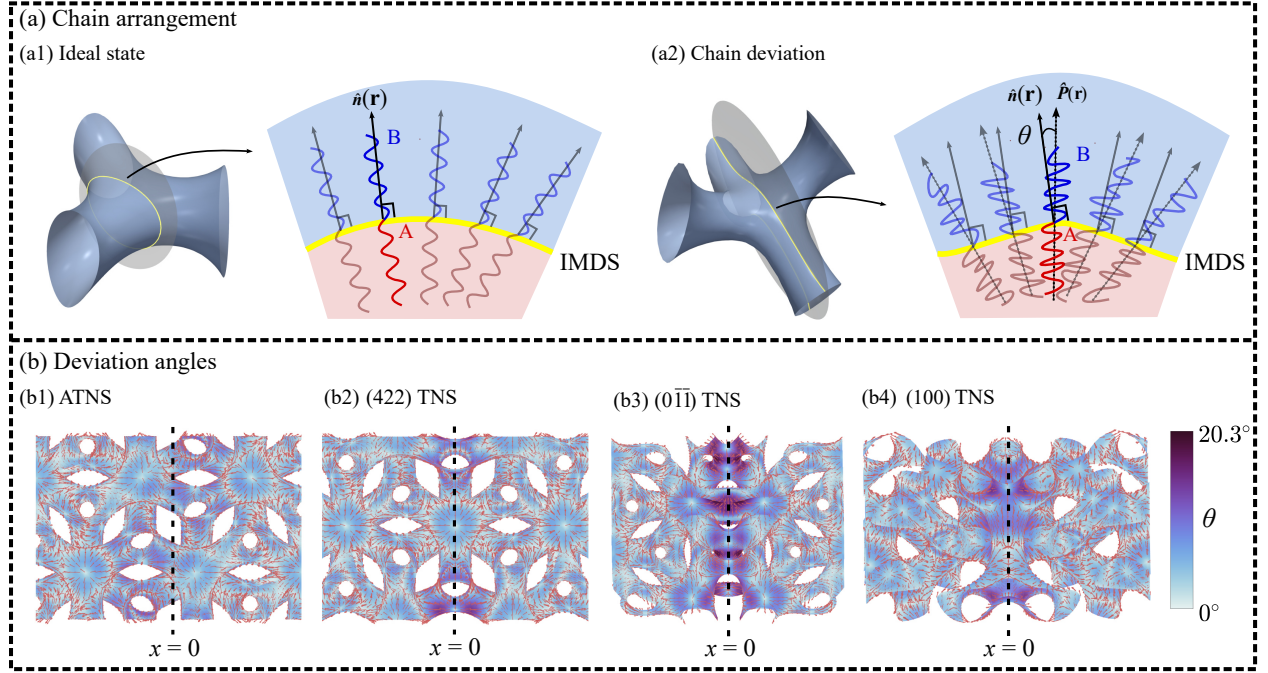


Figure 5: (a) Schematics of chain trajectory packing and the definition of deviation angle θ . (a1) and (a2) depict the chain arrangements in the ideal state and the chain deviation near new nodes, respectively. The deviation angle θ is defined at the isosurface $\phi_A(\mathbf{r}) = 0.5$ as the angle between the normalized polar order parameter $\hat{P}(\mathbf{r})$ and the local surface normal $\hat{n}(\mathbf{r})$. (b) Spatial distributions of the deviation angle θ in the (b1) ATNS, (b2) (422) TNS, (b3) (011) TNS and (b4) (100) TNS. The red arrows represent the deviation vectors projected onto the $\phi_A(\mathbf{r}) = 0.5$ surface, where the arrow length corresponds to the magnitude of the local chain deviation.

As shown in Fig. 4 and Fig. 6, the average chain deviation angle correlates directly with the entropy contribution to the GB energy, while changes in the IMDS area align with the interaction energy. For the ATNS and (422) TNS, both quantities exhibit a weak dependence on composition, consistent with their nearly constant entropy and interaction energies. In contrast, the (011) and (100) TNSs undergo pronounced chain rearrangements as f varies, leading to strong changes in both chain deviation and IMDS area, and consequently larger entropy penalties. Importantly, although the ATNS exhibits a larger IMDS area

than the (422) TNS, resulting in higher interaction energy. It maintains a more relaxed chain conformation with reduced packing frustration (Fig. 6(a)). This entropic advantage outweighs the interaction penalty, rendering the ATNS the most thermodynamically stable GB structure.

The visualization of chain trajectories further supports this mechanism. In the ATNS and (422) TNS, chain aggregation patterns near the interface remain highly consistent with those of the adjoining grains (Fig. 7(a)-(b)), whereas the (0 $\bar{1}\bar{1}$) and (100) TNSs require substantial reorganization of both chain trajectories and A-rich domain morphologies (Fig. 7(c)-(d)). Specifically, chain trajectories in the (0 $\bar{1}\bar{1}$) TNS undergo a transition from the strip-like aggregation of grain 1 to point-like aggregation (Fig. 7(c)), while the (100) TNS transitions from a double short-strip aggregation into a single long-strip aggregation (Fig. 7(d)). These rearrangements introduce significant conformational constraints, providing a clear microscopic origin for the observed entropy penalties.

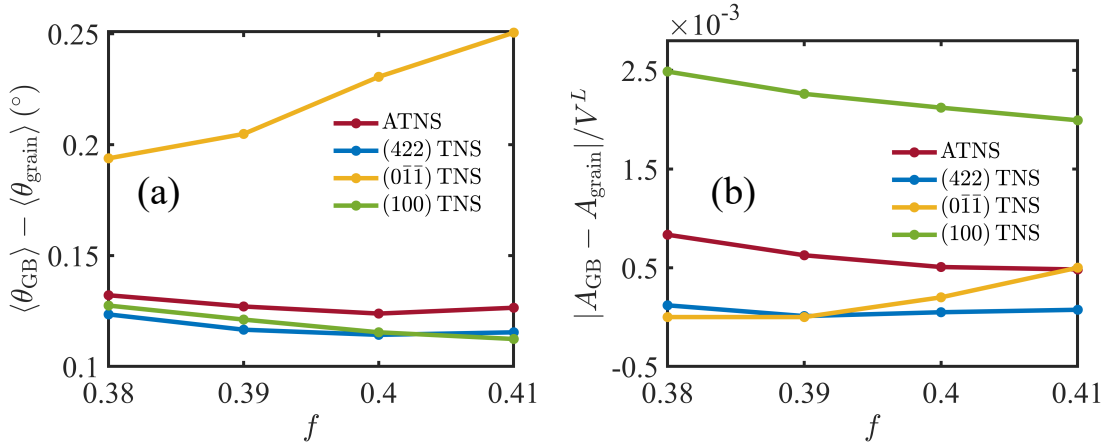


Figure 6: (a) Average chain deviation angle and (b) IMDS area of the GBs with respect to grain 1, as a function of the volume fraction f .

GB Network Topologies

Based on chain-trajectory analysis, we elucidate the microscopic origins of the energetic hierarchy among DG network-switching GBs. Unlike hard matter, where lattice mismatch

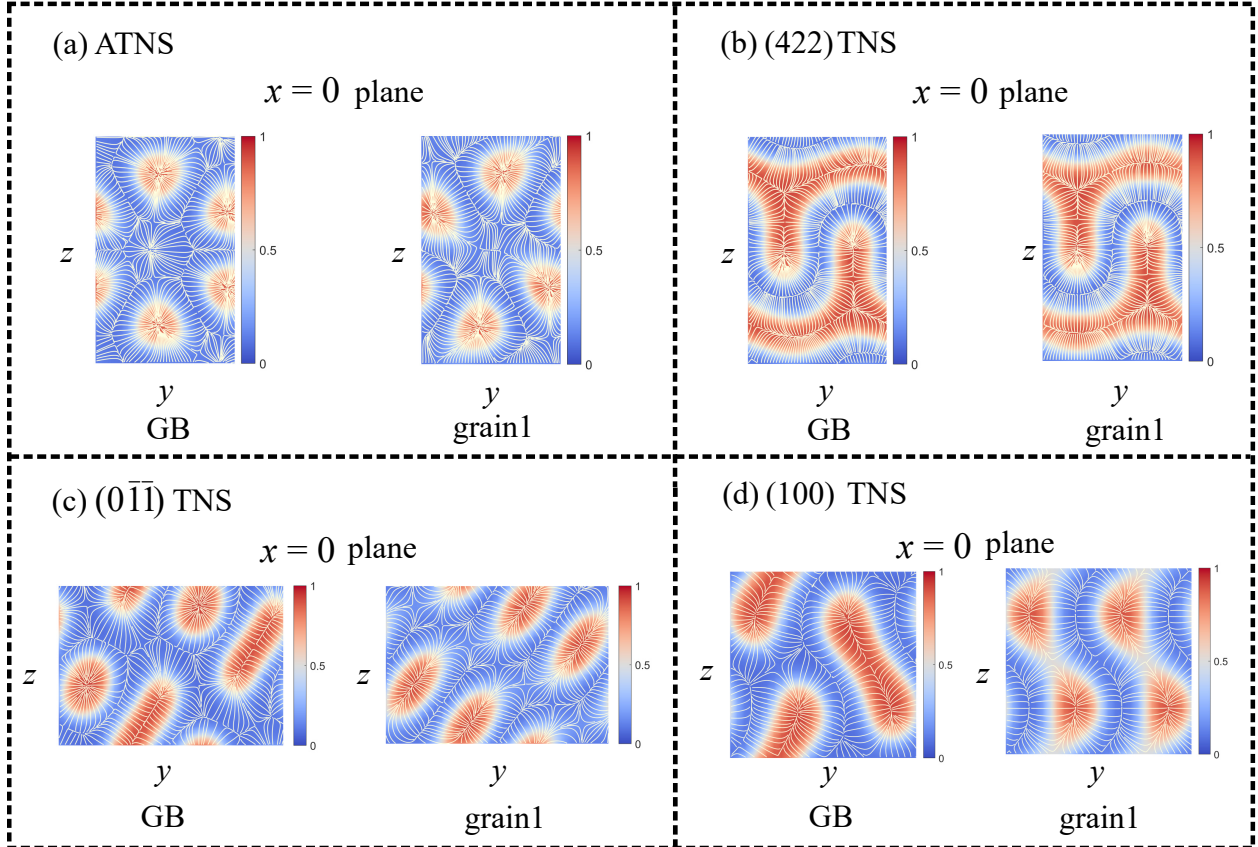


Figure 7: Sections $x = 0$ of chain trajectories for four GBs (left) and the corresponding grain 1 (right) at $f = 0.40$, $\chi N = 14$. The color bar indicates the density distribution of component A.

and elastic distortion dominate GB energies, soft network phases possess an additional degree of freedom, *i.e.* network-topology reconstruction. This unique feature enables stress relaxation through geometric deformation and topological rearrangements. A notable feature common to all four GBs studied here is the switching of network handedness near the GB region, reflecting the intrinsic topological flexibility of the DG network. Therefore, we proceed to a comparative analysis of these GB structures from a topological perspective. All results in this section are obtained at fixed SCFT parameters $f = 0.40$ and $\chi N = 14$. For all mirror-symmetric GBs discussed below, including (422), $(0\bar{1}\bar{1})$ and (100) TNS, their mirror symmetries are verified by ensuring that the density difference satisfies $|\phi_{A,GB}(x, y, z) - \phi_{A,GB}(-x, y, z)| < 10^{-13}$.

Asymmetric tilt network-switching (ATNS) GB

Among the four investigated DG network-switching GBs, the ATNS exhibits the highest thermodynamic stability. Its network topologies are illustrated in Fig. 8. Due to the 180° rotational symmetry of the two grains about the $[\bar{1}\bar{1}1]$ axis, it is sufficient to analyze one network branch. Nodes are labeled by numbers, where identical labels assigned to equivalent positions across periods. At the contact plane ($x = 0$), the networks of opposing chirality reconnect directly through existing struts, without the formation of new nodes. This connection produces eight circuits that traverse the $x = 0$ plane, containing nine, ten, and eleven nodes, respectively (Fig. 8 (b)).

Although the chirality reversal induces some distortions in the strut lengths and angles near the interface, these deformations remain spatially localized. Specifically, struts crossing the $x = 0$ plane (e.g., 1-2, 7-8) deviate less than 6% from the bulk length ($0.35a$), whereas those near $x = 0$ (e.g., 6-7, 1-9, 1-10, 7-12) undergo larger deformations. Strut angles and dihedral angles also change slightly near $x = 0$ (Fig. 8 (c), (d)). In the bulk DG, each node lies in a plane named by its three neighboring nodes. This node coplanarity is well-preserved in the ATNS, with deviations remaining below 4% even near $x = 0$ (Fig. 8 (d)). The sums of

multiple sets of adjacent dihedral angles are close to 180° (e.g., dihedral angles 1-(2,3)-12, 1-(2,12)-3, and 17-(15,14)-10). Such preservation of coplanarity and strut-mediated connection allow polymer chains to accommodate network switching through smooth redistribution of contour length and local torsion, rather than through severe bending or orientational confinement. As a result, the ATNS accommodates network reconnection with the minimal chain packing frustration, leading to a small entropy penalty and explaining its superior thermodynamic stability.

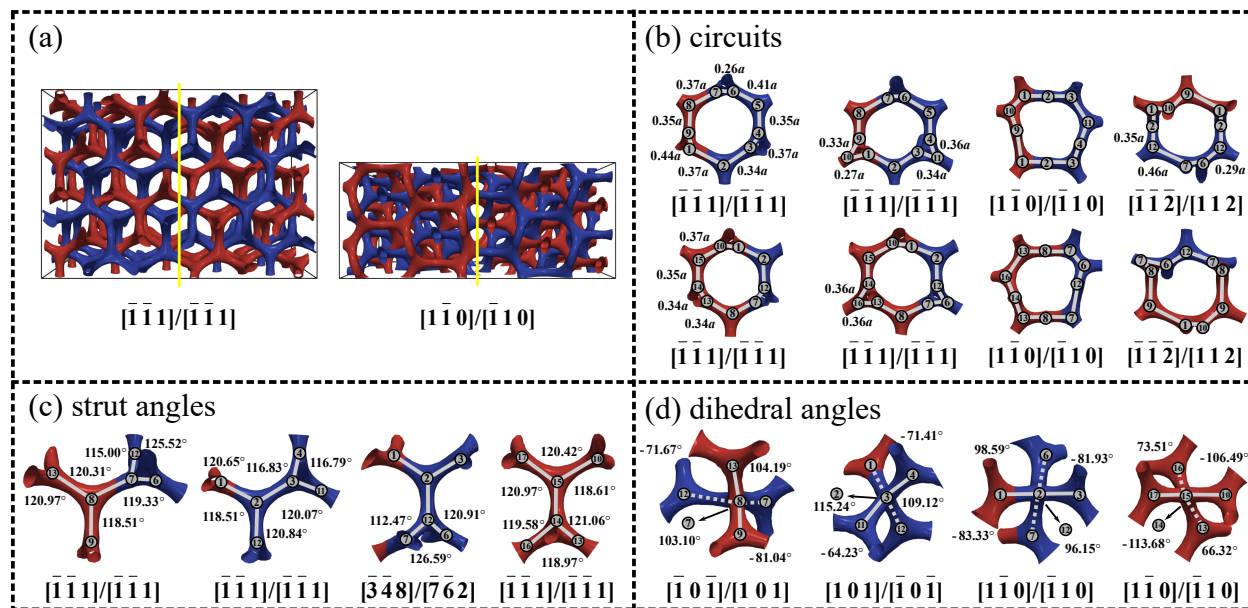


Figure 8: (a) ATNS skeletons. (b)-(d) Circuits, strut angles and dihedral angles.

(422) twist network-switching (TNS) GB

The (422) TNS is slightly higher in GB energy than the ATNS and exhibits a distinct reconnection mechanism, as shown in Fig. 9. At the contact plane, reconnection between the two grains generates three types of new nodes, including a four-connected node (labeled blue 1) and two three-connected nodes (labeled green 2 and orange 3). The circuits associated with these new nodes are classified into two categories, single-circuit and double-circuit. The former arise from direct connections between grains through the new nodes (Fig. 9 (b1)-(b3)), while the latter occur when the circuits from both grains share the new nodes (Fig. 9 (b4)-

(b9)). Due to the mirror symmetry, only half of the strut lengths are labeled in each circuit. These network topologies are consistent with previous studies.^{40,43}

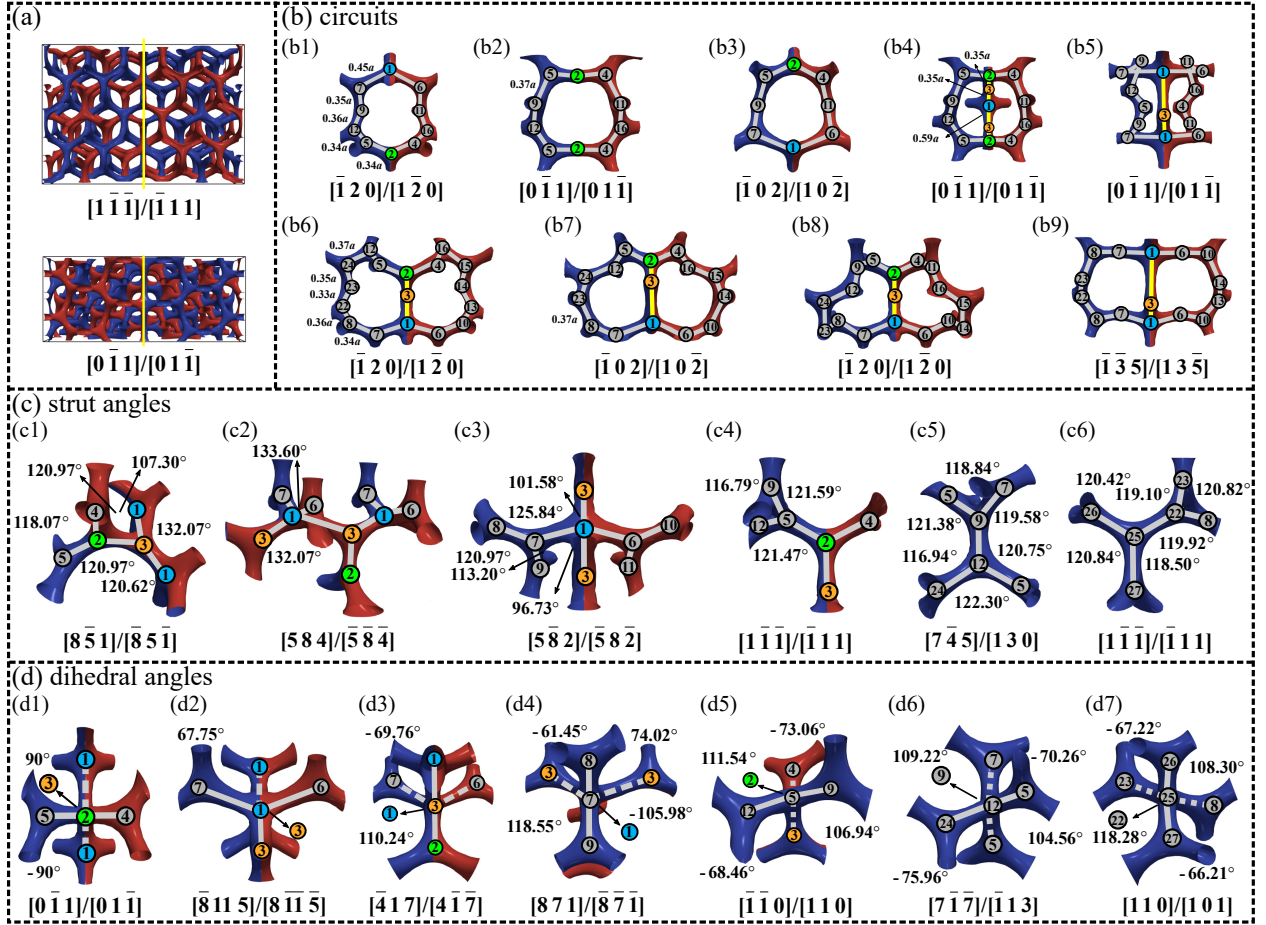


Figure 9: (a) (422) TNS skeletons. (b)-(d) Circuits, strut angles, and dihedral angles.

The newly formed nodes lead to pronounced geometric reconstruction in their vicinity (Fig. 9 (b)-(d)). Most struts deviate by less than 6% from the bulk length, except for struts 1-3 and 1-7 connected to the four-connected Node 1, which show substantial deviation (exceeding 28%, Fig. 9 (b)). For instance, the notable elongation of strut 1-3 to $0.59a$ results from the inward offset and fusion of two struts from two grains. Similarly, strut angles involving Node 1 deviate substantially, exceeding 10% from the ideal 120° (Fig. 9 (c1)-(c3)). Significant deviations of dihedral angles occur when new nodes are involved, and vertical planes appear (Fig. 9 (d1)). The network chirality reverses locally, as indicated by dihedral angles (Fig. 9 (d2), (d4)). The node coplanarity is preserved only in partial regions. Specifi-

cally, when only one new node on $x = 0$ is involved, coplanarity can be well maintained (see dihedral angles 8-(7,1)-9, 9-(5,2)-12 in Fig. 9 (d4)-(d5)), while regions without new nodes also display small deviations below 4% of 180° (see Fig. 9 (d6)-(d7)). Compared with the ATNS, the (422) TNS incurs an additional entropic cost associated with new-node generation and partial breakdown of coplanarity, accounting for its higher GB energy despite its well-known stability in hard matter.

$(0\bar{1}\bar{1})$ twist network-switching (TNS) GB

We next examine the $(0\bar{1}\bar{1})$ TNS, a high-energy configuration characterized by extensive topological reconstruction at the GB region. In contrast to the (422) TNS, the chirality switching in the $(0\bar{1}\bar{1})$ TNS induces complex node fusion and splitting events, generating three types of new nodes (marked green, yellow and cyan in Fig. 10 (b)). These reconstructed nodes and their connecting struts form two categories of circuits (Fig. 10 (c)), single-circuits (c1)-(c4) and double-circuits (c5)-(c6). The geometric distortions associated with this reconstructions become severe. Strut lengths connected to new nodes exhibit large contractions, with strut angles and dihedral angles deviating markedly from their bulk values. Most importantly, the node coplanarity is extensively destroyed, not only at the contact plane but also in regions far from the interface.

Specifically, struts involving two new nodes shorten by over 34% from $0.35a$ (see struts 39-40 and 28-32 in Fig. 10 (c5)-(c6)), while those containing a single new node typically shorten by over 14%, except for struts 1-7 and 5-14 (Fig. 10 (c1)). Significant structural distortions occur in network (b2) (Fig. 10 (b2)), with deviations in network (b1) remaining below 9% and 8% for strut angles and coplanarity, respectively. Consequently, we only show the angular deformations in network (b2) as illustrated in Fig. 10 (d)-(e). Strut angles (Fig. 10 (d1), (d2), (d4)) and dihedral angles (Fig. 10 (e1)-(e7)) involving new nodes exhibit substantial deformations, while dihedral angles deviate more than strut angles. If the new nodes are considered as vertices, the deformations of most strut angles exceed 16%

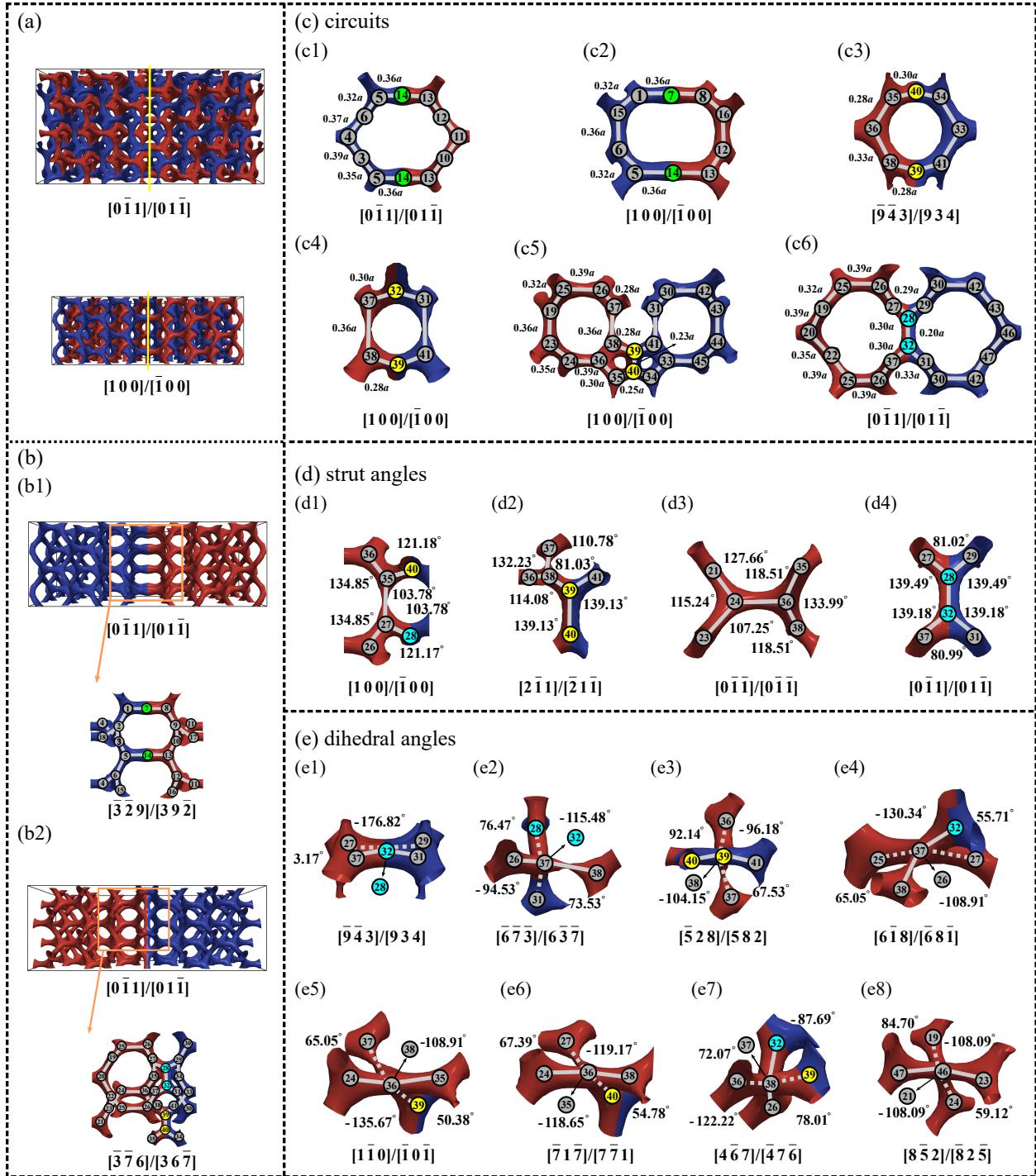


Figure 10: (a) $(0\bar{1}\bar{1})$ TNS skeletons. (b) Two networks. (c)-(e) Circuits, strut angles, and dihedral angles.

(Fig. 10 (d2), (d4)). When nodes connected to $x = 0$ (nodes 27 and 38) are involved, geometric parameters change to a greater extent than in the (422) TNS. For example, the strut angles 37-38-36, 35-36-38 in Fig. 10 (d2), (d4) and dihedral angles 38-36-35-27, 36-38-37-26 in Fig. 10 (e6)-(e7) occur large deviations. Even far away from $x = 0$, some dihedral angles still vary clearly (an example is angle 47-46-21-19 in Fig. 10 (e8)). Furthermore, the coplanarity is also largely broken, as can be seen in dihedral angles 37-(32,28)-31, 32-(37,26)-38, and 39-(38,36)-37 (Fig. 10 (e1), (e4), (e5)). The fusion and splitting of new nodes, and the widespread breakdown of coplanarity, impose strong orientational and bending constraints on flexible polymer chains. This leads to intense chain packing frustration and a large entropy penalty. Consequently, the $(0\bar{1}\bar{1})$ TNS exhibits a higher GB energy than both the ATNS and the (422) TNS.

(100) **twist network-switching (TNS) GB**

Finally, we analyze the (100) TNS, which possesses the highest GB energy among the four configurations. As illustrated in Fig. 11, although its topological reconstruction involves fewer new nodes than the $(0\bar{1}\bar{1})$ TNS, the associated geometric distortions, particularly the breakdown of node coplanarity, are more pronounced. At the contact plane, the interconnection of the two chiral networks generates two new nodes (labeled green 1 and yellow 2 in Fig. 11 (b)), leading to the formation of three circuits, including single-circuits (b1)-(b2) and double-circuits (b3).

Similar to the $(0\bar{1}\bar{1})$ TNS, the (100) TNS undergoes severe structural distortions stemming from its topological reconstructions. Notably, the newly formed strut 1-2 exhibits a pronounced elongation of 41% (Fig. 11 (b3)), while its neighbors (1-3 and 2-4) contract by over 18% to alleviate the interfacial geometric mismatch (Fig. 11 (b1)). Such deviations are also reflected in the angular data, where strut angles involving nodes 1 and 2 exhibit significant deviations from bulk values, particularly for angles 7-3-1, 1-3-4, and 2-4-3 in Fig. 11 (c2). Furthermore, the chirality of the network is locally reversed, as indicated by the dihedral

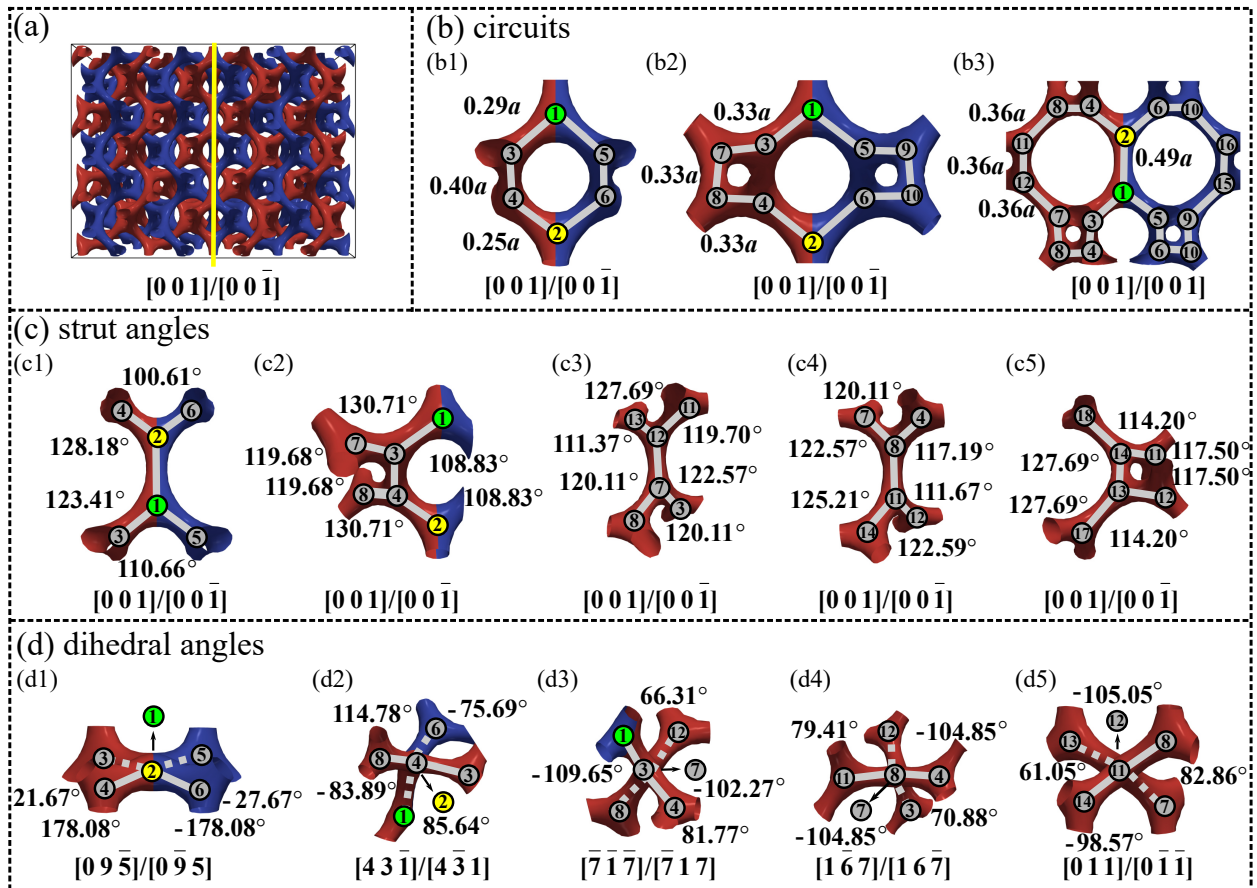


Figure 11: (a) The (100) TNS skeleton. (b)-(d) Circuits, strut angles, and dihedral angles.

angles in Fig. 11 (d1)-(d2).

Most importantly, the (100) TNS exhibits a more severe destruction of node coplanarity than any other configuration. For example, the dihedral angles 4-(2,1)-6 and 3-(1,2)-5 deviate by 13% (Fig. 11 (d1)), exceeding the maximum deviation of 11% observed in the (0 $\bar{1}\bar{1}$) TNS (Fig. 10 (e5)). In the (100) TNS, this breakdown is not limited to instances involving the new nodes (e.g., dihedral angles 4-(2,1)-6, 3-(1,2)-5, 3-(4,2)-8, 1-(3,7)-4 in Fig. 11 (d1)-(d3)). It also extends to cases where involved nodes have at most one connection to $x = 0$, such as 3-(7,8)-12, 4-(8,7)-11, 7-(12,11)-13 (Fig. 11 (d4)-(d5)). This severe disruption of node coplanarity imposes stronger conformational constraints on the polymer chains, leading to a higher entropy penalty and rendering the (100) TNS the least thermodynamically stable configuration.

Geometric Deformation Statistics

To quantitatively correlate geometric deformation with GB stability, we analyze the maximum geometric deviations in strut lengths, strut angles, dihedral angles, and node coplanarity for the four DG GBs (Tab. 2). The statistical data spans two grain periods along x -direction (centered at $x = 0$) and one period along both y and z directions. We evaluate node coplanarity by measuring the maximum deviation of the dihedral angles formed by three planes, each defined by the node and its two connecting nodes. We then partition the nodes into three distinct spatial regions. Region I corresponds to nodes on $x = 0$, region N to nodes with a strut touching or crossing $x = 0$, and region F to the remaining nodes. This classification applies to strut lengths and angles, with elements assigned to region I if constituent node lies there, to region N if node lies in N (but not I), and to region F otherwise. In the statistical analysis of dihedral angle deviations, we consider only the geometric deformation of struts pre-existing in the original bulk grain structures, excluding metrics associated with newly generated struts.

The statistical results reveal a clear distinction between low- and high-energy GBs. For

Table 2: Maximum variations for strut lengths, dihedral angles, strut angles, coplanarity.

GBs	Region	Strut length ($0.35a$)	Strut angle (120°)	Dihedral angle ($\pm 70.5^\circ$)	Coplanarity (180°)
ATNS	N	$\pm 0.11a$	$\pm 8.15^\circ$	$\pm 13.35^\circ$	$\pm 6.65^\circ$
	F	$\pm 0.06a$	$\pm 7.69^\circ$	$\pm 9.76^\circ$	$\pm 7.19^\circ$
(422) TNS	I	$\pm 0.24a$	$\pm 23.27^\circ$	$\pm 35.48^\circ$	$\pm 69.76^\circ$
	N	$\pm 0.02a$	$\pm 3.58^\circ$	$\pm 4.94^\circ$	$\pm 5.18^\circ$
	F	$\pm 0.02a$	$\pm 6.57^\circ$	$\pm 8.78^\circ$	$\pm 6.32^\circ$
(0 $\bar{1}\bar{1}$) TNS	I	$\pm 0.15a$	$\pm 16.22^\circ$	$\pm 26.17^\circ$	$\pm 20.72^\circ$
	N	$\pm 0.07a$	$\pm 14.85^\circ$	$\pm 12.72^\circ$	$\pm 8.33^\circ$
	F	$\pm 0.04a$	$\pm 12.75^\circ$	$\pm 14.21^\circ$	$\pm 12.79^\circ$
(100) TNS	I	$\pm 0.14a$	$\pm 11.17^\circ$	$\pm 25.61^\circ$	$\pm 23.60^\circ$
	N	$\pm 0.05a$	$\pm 5.80^\circ$	$\pm 11.27^\circ$	$\pm 9.56^\circ$
	F	$\pm 0.02a$	$\pm 8.63^\circ$	$\pm 12.36^\circ$	$\pm 13.90^\circ$

the three twist-type GBs, there exists a I-region at the GB center, where new node generation and topological reconstruction are most concentrated, leading to pronounced geometric deformation. In contrast, the ATNS lacks this region, and its minimal distortions are distributed across the N- and F-regions. The emergence of the I-region forces chain segments to rearrange under new nodes, inevitably introducing chain packing frustration and entropic penalties. This reconstruction-induced conformational constraint is the primary source of the high energy in twist GBs. Conversely, the ATNS connects two grains via existing struts without generating new nodes, allowing chains to remain relatively relaxed with higher conformational freedom. A comparative analysis of the N- and F-regions reveals that in the lower-energy ATNS and (422) TNS, strut length and dihedral angle are more prone to change compared to strut angle and node coplanarity, with several deviations exceeding 6%. This suggests that chains alleviate geometric mismatch through chain length redistribution and local torsion to preserve node coplanarity, thereby maximizing conformational freedom. Notably, among all geometric parameters considered, node coplanarity consistently shows the smallest deviation in low-energy GBs (within 6%). This highlights coplanarity as the critical geometric constraint for maintaining low GB energy, as it represents the relaxed, unconstrained arrangement for chains at the nodes. This conclusion is further validated

by high-energy GBs. Although the maximum deviations in strut length and angles for the (100) TNS are smaller than those for the $(0\bar{1}\bar{1})$ TNS, its node coplanarity is more severely disrupted. This significant distortion of coplanarity forces chains to undergo intense bending and orientational constraints, leading to a sharp increase in the entropy penalty and GB energy. These results demonstrate that the stability of network-phase GBs is governed by entropy, with new node deformation and node coplanarity serving as the critical geometric indicator of a low-entropy-penalty configuration.

Conclusion

In this work, we have developed a SCFT framework specifically designed for investigating GBs in ordered phases of BCPs, together with an accurate and efficient numerical method for computing GB energies. Within this framework, we establish a comprehensive GB energy landscape for the DG phase, providing a global perspective on GB configurations and highlighting network switching as a key characteristic governing GB energetics. The energy landscape further shows that a previously unidentified asymmetric tilt network-switching GB (ATNS) emerges as the global minimum, surpassing the experimentally reported (422) TNS. Guided by the energy landscape, we select four representative network-switching GBs for detailed investigations, including the low-energy ATNS, (422) TNS, together with two higher-energy twist GBs ((100) and $(0\bar{1}\bar{1})$ TNSs) for comparative analyses. GB energy decomposition demonstrates that the stability of GBs in BCP network phases is predominantly governed by the entropy contribution.

Detailed analyses of chain trajectories, IMDS geometry, and network topology elucidate the microscopic origin of this stability. For twist-type GBs, the formation of new nodes and the disruption of node coplanarity impose strong conformational and orientational constraints on polymer chains, leading to severe packing frustration and large entropy penalties. In contrast, the ATNS connects two grains via existing struts, avoiding new-node generation

and largely preserving node coplanarity. This allows geometric mismatch to be accommodated through relaxed conformation adjustment, thereby minimizing entropy penalty and yielding superior thermodynamic stability. These findings reveal an entropy-driven physical mechanism for GB stability in soft-matter network phases. Low-energy GBs are selected by minimizing entropy penalties, notably the avoidance of new-node formation and the preservation of nodal coplanarity, rather than by strict lattice matching.

More broadly, this work provides a theoretical framework and guiding principles for understanding and engineering defects in complex soft-matter networks, offering insights into a wide class of self-assembled materials.

Acknowledgement

This work is supported by the National Key R&D Program of China (2023YFA1008802), the Science and Technology Innovation Program of Hunan Province (2024RC1052), the Innovative Research Group Project of Natural Science Foundation of Hunan Province of China (2024JJ1008), the Natural Sciences and Engineering Research Council of Canada, the Postgraduate Scientific Research Innovation Project of Hunan Province (CX20240589), the Postgraduate Scientific Research Innovation Project of Xiangtan University (XDCX2025Y237), and the High Performance Computing Platform of Xiangtan University.

References

- (1) Bates, F. S.; Fredrickson, G. H. Block copolymers—designer soft materials. *Physics today* **1999**, *52*, 32–38.
- (2) Hajduk, D. A.; Harper, P. E.; Gruner, S. M.; Honeker, C. C.; Kim, G.; Thomas, E. L.; Fetters, L. J. The gyroid: a new equilibrium morphology in weakly segregated diblock copolymers. *Macromolecules* **1994**, *27*, 4063–4075.

- (3) Roy, R.; Park, J. K.; Young, W.-S.; Mastroianni, S. E.; Tureau, M. S.; Epps III, T. H. Double-gyroid network morphology in tapered diblock copolymers. *Macromolecules* **2011**, *44*, 3910–3915.
- (4) Chang, C.-Y.; Manesi, G.-M.; Yang, C.-Y.; Hung, Y.-C.; Yang, K.-C.; Chiu, P.-T.; Avgeropoulos, A.; Ho, R.-M. Mesoscale networks and corresponding transitions from self-assembly of block copolymers. *Proceedings of the National Academy of Sciences* **2021**, *118*, e2022275118.
- (5) Asai, Y.; Suzuki, J.; Aoyama, Y.; Nishioka, H.; Takano, A.; Matsushita, Y. Tricontinuous double diamond network structure from binary blends of ABC triblock terpolymers. *Macromolecules* **2017**, *50*, 5402–5411.
- (6) Bailey, T. S.; Hardy, C. M.; Epps, T. H.; Bates, F. S. A noncubic triply periodic network morphology in poly (isoprene-b-styrene-b-ethylene oxide) triblock copolymers. *Macromolecules* **2002**, *35*, 7007–7017.
- (7) Epps, T. H.; Cochran, E. W.; Hardy, C. M.; Bailey, T. S.; Waletzko, R. S.; Bates, F. S. Network phases in ABC triblock copolymers. *Macromolecules* **2004**, *37*, 7085–7088.
- (8) Maldovan, M.; Urbas, A.; Yufa, N.; Carter, W.; Thomas, E. Photonic properties of bicontinuous cubic microphases. *Physical Review B* **2002**, *65*, 165123.
- (9) Urbas, A. M.; Maldovan, M.; DeRege, P.; Thomas, E. L. Bicontinuous cubic block copolymer photonic crystals. *Advanced Materials* **2002**, *14*, 1850–1853.
- (10) Saba, M.; Thiel, M.; Turner, M. D.; Hyde, S.; Gu, M.; Grosse-Brauckmann, K.; Neshchev, D. N.; Mecke, K.; Schröder-Turk, G. E. Circular dichroism in biological photonic crystals and cubic chiral nets. *Physical Review Letters* **2011**, *106*, 103902.
- (11) Goto, K.; Rozhanskii, I.; Yamakawa, Y.; Otsuki, T.; Naito, Y. Development of aro-

- matic polymer electrolyte membrane with high conductivity and durability for fuel cell. *Polymer journal* **2009**, *41*, 95–104.
- (12) Prasad, I.; Jinnai, H.; Ho, R.-M.; Thomas, E. L.; Grason, G. M. Anatomy of triply-periodic network assemblies: characterizing skeletal and inter-domain surface geometry of block copolymer gyroids. *Soft Matter* **2018**, *14*, 3612–3623.
- (13) Oh, S. S.; Demetriadou, A.; Wuestner, S.; Hess, O. On the origin of chirality in nanoplasmonic gyroid metamaterials. *Advanced Materials (Deerfield Beach, Fla.)* **2012**, *25*, 612–617.
- (14) Lee, J.-H.; Koh, C. Y.; Singer, J. P.; Jeon, S.-J.; Maldovan, M.; Stein, O.; Thomas, E. L. 25th anniversary article: Ordered polymer structures for the engineering of photons and phonons. *Advanced Materials* **2014**, *26*, 532–569.
- (15) Hur, K.; Francescato, Y.; Giannini, V.; Maier, S. A.; Hennig, R. G.; Wiesner, U. Three-dimensionally isotropic negative refractive index materials from block copolymer self-assembled chiral gyroid networks. *Angewandte Chemie International Edition* **2011**, *50*, 11985–11989.
- (16) Li, W.; Müller, M. Defects in the self-assembly of block copolymers and their relevance for directed self-assembly. *Annual review of chemical and biomolecular engineering* **2015**, *6*, 187–216.
- (17) Li, Z.; Hur, K.; Sai, H.; Higuchi, T.; Takahara, A.; Jinnai, H.; Gruner, S. M.; Wiesner, U. Linking experiment and theory for three-dimensional networked binary metal nanoparticle–triblock terpolymer superstructures. *Nature communications* **2014**, *5*, 3247.
- (18) Feng, X.; Guo, H.; Thomas, E. L. Topological defects in tubular network block copolymers. *Polymer* **2019**, *168*, 44–52.

- (19) Feng, X.; Burke, C. J.; Zhuo, M.; Guo, H.; Yang, K.; Reddy, A.; Prasad, I.; Ho, R.-M.; Avgeropoulos, A.; Grason, G. M.; others Seeing mesoatomic distortions in soft-matter crystals of a double-gyroid block copolymer. *Nature* **2019**, *575*, 175–179.
- (20) Miyata, T.; Wang, H.-F.; Suenaga, T.; Watanabe, D.; Marubayashi, H.; Jinnai, H. Dislocation-induced defect formation in a double-gyroid network. *Macromolecules* **2022**, *55*, 8143–8149.
- (21) Shan, W.; Subramanian, V.; Feng, X.; Thomas, E. L. The nature of crystallographic defects in noncrystalline tubular network block copolymers. *Giant* **2024**, *17*, 100216.
- (22) Sutton, A. P.; Balluffi, R. W. *Interfaces in Crystalline Materials*; Oxford University Press: Oxford, UK, 1995.
- (23) Gottstein, G.; Shvindlerman, L. S. *Grain boundary migration in metals: thermodynamics, kinetics, applications*; CRC press, 2009.
- (24) Murdoch, H. A.; Schuh, C. A. Estimation of grain boundary segregation enthalpy and its role in stable nanocrystalline alloy design. *Journal of Materials Research* **2013**, *28*, 2154–2163.
- (25) Read, W. T.; Shockley, W. Dislocation models of crystal grain boundaries. *Physical review* **1950**, *78*, 275.
- (26) Bulatov, V. V.; Reed, B. W.; Kumar, M. Grain boundary energy function for fcc metals. *Acta Materialia* **2014**, *65*, 161–175.
- (27) Tschopp, M. A.; Coleman, S. P.; McDowell, D. L. Symmetric and asymmetric tilt grain boundary structure and energy in Cu and Al (and transferability to other fcc metals). *Integrating Materials and Manufacturing Innovation* **2015**, *4*, 176–189.
- (28) Hahn, E. N.; Fensin, S. J.; Germann, T. C.; Meyers, M. A. Symmetric tilt boundaries in body-centered cubic tantalum. *Scripta Materialia* **2016**, *116*, 108–111.

- (29) Li, S.; Yang, L.; Lai, C. Atomistic simulations of energies for arbitrary grain boundaries. Part I: Model and validation. *Computational Materials Science* **2019**, *161*, 330–338.
- (30) Gido, S. P.; Gunther, J.; Thomas, E. L.; Hoffman, D. Lamellar diblock copolymer grain boundary morphology. 1. Twist boundary characterization. *Macromolecules* **1993**, *26*, 4506–4520.
- (31) Gido, S. P.; Thomas, E. L. Lamellar diblock copolymer grain boundary morphology. 4. Tilt boundaries. *Macromolecules* **1994**, *27*, 6137–6144.
- (32) Carvalho, B. L.; Lescanec, R. L.; Thomas, E. L. Grain boundary defects in block copolymer systems: Bulk and thin film results. *Macromolecular Symposia*. 1995; pp 1131–1146.
- (33) Jinnai, H.; Sawa, K.; Nishi, T. Direct observation of twisted grain boundary in a block copolymer lamellar nanostructure. *Macromolecules* **2006**, *39*, 5815–5819.
- (34) Ryu, H. J.; Fortner, D. B.; Lee, S.; Ferebee, R.; De Graef, M.; Misichronis, K.; Avgeropoulos, A.; Bockstaller, M. R. Role of grain boundary defects during grain coarsening of lamellar block copolymers. *Macromolecules* **2013**, *46*, 204–215.
- (35) Han, L.; Xiong, P.; Bai, J.; Che, S. Spontaneous formation and characterization of silica mesoporous crystal spheres with reverse multiply twinned polyhedral hollows. *Journal of the American Chemical Society* **2011**, *133*, 6106–6109.
- (36) Han, L.; Fujita, N.; Chen, H.; Jin, C.; Terasaki, O.; Che, S. Crystal twinning of bicontinuous cubic structures. *IUCrJ* **2020**, *7*, 228–237.
- (37) Liu, H.-K.; Ma, Y.-L.; Ren, L.-J.; Kübel, C.; Wang, W. Symmetry and topology of twin boundaries and five-fold twin boundaries in soft crystals. *Langmuir* **2021**, *37*, 10291–10297.

- (38) Feng, X.; Dimitriyev, M. S.; Thomas, E. L. Soft, malleable double diamond twin. *Proceedings of the National Academy of Sciences* **2023**, *120*, e2213441120.
- (39) Vignolini, S.; Yufa, N. A.; Cunha, P. S.; Guldin, S.; Rushkin, I.; Stefik, M.; Hur, K.; Wiesner, U.; Baumberg, J. J.; Steiner, U. A 3D Optical Metamaterial Made by Self-Assembly. *Advanced Materials* **2011**, *24*, OP23–OP27.
- (40) Feng, X.; Zhuo, M.; Guo, H.; Thomas, E. L. Visualizing the double-gyroid twin. *Proceedings of the National Academy of Sciences* **2021**, *118*, e2018977118.
- (41) Chen, H. Minimal Twin Surfaces. *Experimental Mathematics* **2018**, *28*, 404–419.
- (42) Belushkin, M.; Gompper, G. Twist grain boundaries in cubic surfactant phases. *The Journal of chemical physics* **2009**, *130*.
- (43) Chen, J.; Jiang, K.; Sun, Z.; Xu, J. Computational Method of Grain Boundary Energy Consistent for Different Orientations and Applications to Double Gyroid Beyond Twinning. *Communications in Computational Physics* **2025**, *39*, 9.
- (44) Fredrickson, G. *The equilibrium theory of inhomogeneous polymers*; Oxford University Press, 2006.
- (45) Matsen, M. W.; Schick, M. Stable and unstable phases of a diblock copolymer melt. *Physical Review Letters* **1994**, *72*, 2660.
- (46) Matsen, M. W. The standard Gaussian model for block copolymer melts. *Journal of Physics: Condensed Matter* **2001**, *14*, R21.
- (47) Duan, C.; Zhao, M.; Qiang, Y.; Chen, L.; Li, W.; Qiu, F.; Shi, A.-C. Stability of two-dimensional dodecagonal quasicrystalline phase of block copolymers. *Macromolecules* **2018**, *51*, 7713–7721.
- (48) Wang, X.; Shi, A.-C.; Zhang, P.; Jiang, K. Stability of diverse dodecagonal quasicrystals in T-shaped liquid crystalline molecules. *Macromolecules* **2025**, *58*, 5229–5239.

- (49) Gido, S. P.; Thomas, E. L. Lamellar diblock copolymer grain boundary morphology. 2. Scherk twist boundary energy calculations. *Macromolecules* **1994**, *27*, 849–861.
- (50) Gido, S. P.; Thomas, E. L. Lamellar diblock copolymer grain boundary morphology. 3. Helicoid section twist boundary energy. *Macromolecules* **1997**, *30*, 3739–3746.
- (51) Hashimoto, T.; Koizumi, S.; Hasegawa, H. Ordered structure in blends of block copolymers. 2. Self-assembly for immiscible lamella-forming copolymers. *Macromolecules* **1994**, *27*, 1562–1570.
- (52) Matsen, M. Kink grain boundaries in a block copolymer lamellar phase. *The Journal of chemical physics* **1997**, *107*, 8110–8119.
- (53) Duque, D.; Schick, M. Self-consistent field theory of twist grain boundaries in block copolymers. *The Journal of Chemical Physics* **2000**, *113*, 5525–5530.
- (54) Jiang, K.; Xu, W.; Zhang, P. Analytic structure of the SCFT energy functional of multicomponent block copolymers. *Communications in Computational Physics* **2015**, *17*, 1360–1387.
- (55) Cochran, E. W.; Garcia-Cervera, C. J.; Fredrickson, G. H. Stability of the gyroid phase in diblock copolymers at strong segregation. *Macromolecules* **2006**, *39*, 2449–2451.
- (56) Jiang, K.; Huang, Y.; Zhang, P. Spectral method for exploring patterns of diblock copolymers. *Journal of Computational Physics* **2010**, *229*, 7796–7805.
- (57) Thompson, R. B.; Rasmussen, K. O.; Lookman, T. Improved convergence in block copolymer self-consistent field theory by Anderson mixing. *The Journal of chemical physics* **2004**, *120*, 31–34.
- (58) Jiang, K.; Zhang, J.; Liang, Q. Self-assembly of asymmetrically interacting ABC star triblock copolymer melts. *The Journal of Physical Chemistry B* **2015**, *119*, 14551–14562.

- (59) Frigo, M.; Johnson, S. The design and implementation of FFTW3. *Proc. IEEE* **2005**, *93*, 216–231.
- (60) Wang, X.; Wang, L.; Jiang, K. Self-consistent field theory simulation platform for polymer phase behavior MPI version (MSCFT) 1.0. National Copyright Administration of the People’s Republic of China, 2025SR2414215, 2025; <https://github.com/wanglizhi02/Self-Consistent-Field-Theory-MPI>.
- (61) Matsen, M. W. Effect of architecture on the phase behavior of AB-type block copolymer melts. *Macromolecules* **2012**, *45*, 2161–2165.
- (62) Greenvall, B. R.; Dimitriyev, M. S.; Grason, G. M. Chain trajectories, domain shapes, and terminal boundaries in block copolymers. *Journal of Polymer Science* **2024**, *62*, 3737–3755.
- (63) Dimitriyev, M. S.; Reddy, A.; Grason, G. M. Medial Packing, Frustration, and Competing Network Phases in Strongly Segregated Block Copolymers. *Macromolecules* **2023**, *56*, 7184–7202.